Electronic Supplementary Material (ESI) for Energy Advances.

Assessing alkyl side chain effects on electron transport properties of Y6–derived non–fullerene acceptors

Daniele Padula,[a*] Alessandro Landi,[b†] Giacomo Prampolini[c‡]

[a] *Dipartimento di Biotecnologie, Chimica e Farmacia, Università di Siena, Via A. Moro 2, I-53100 Siena, Italy*

[b] *Dipartimento di Chimica e Biologia Adolfo Zambelli, Università di Salerno, Via Giovanni Paolo II, I-84084 Fisciano (SA), Italy*

[c] *Istituto di Chimica dei Composti OrganoMetallici (ICCOM-CNR), Area della Ricerca, Via G. Moruzzi 1, I-56124 Pisa, Italy*

Supporting Information

*To whom correspondence should be addressed. Email: daniele.padula@unisi.it

†To whom correspondence should be addressed. Email: alelandi1@unisa.it

‡To whom correspondence should be addressed. Email: giacomo.prampolini@pi.iccom.cnr.it

Contents

List of Figures

List of Tables

S1 Computational details

S1.1 Crystal structures

We retrieved the crystal structure for Y6 from the Supporting Information of ref. 1, and the crystal structures for L8-BO, L8-HD, and L8-OD from the Cambridge Structural Database (CSD)[2] (entries 2005533, 2005534, and 2005535 respectively).[3] We highlight that other crystal structures are available for Y6, but they have either incomplete or no alkyl side chains.[4,5]

S1.2 QMD-FFs parameterisation protocol

All QMD-FFs were parameterized by partioning the total energy of the system in an intramolecular term, governing the flexibility and shape of each monomer, and an intermolecular term, which describes the interactions among different monomers:

$$E_{tot}^{QMD-FF} = E_{intra}^{QMD-FF} + E_{inter}^{QMD-FF} \; ; \; where \tag{S1}$$

$$E_{intra}^{QMD-FF} = \sum_{i=1}^{N_{mol}} u_i^{intra} \; , \; E_{inter}^{QMD-FF} = \sum_{i=1}^{N_{at}} \sum_{i=j}^{N_{at}} u_{ij}^{inter} \tag{S2}$$

with N_{mol}/N_{at} being the number molecules/atoms composing the systems, i and j dummy indexes running over the atoms of two different molecules. For the QMD-FF intramolecular term we adopt a class I expression:

$$\begin{aligned} u^{intra} = \frac{1}{2}\sum_{s}^{N_s} k_s(r-r^0)^2 + \frac{1}{2}\sum_{b}^{N_b} k_b(\theta-\theta^0)^2 + \frac{1}{2}\sum_{st}^{N_{st}} k_{st}(\phi-\phi^0)^2 + \\ \sum_{\mu}^{N_{ft}} \sum_{j}^{N_{cos_\mu}} k_{j\mu}^{ft}\left[1+cos(n_j^\mu \delta_\mu - \gamma_j^\mu)\right] + \\ \sum_{i=1}^{N_{pairs}} \sum_{j=1}^{N_{pairs}} \left(4\epsilon_{ij}^{intra} \left[\left(\frac{\sigma_{ij}^{intra}}{r_{ij}} \right)^{12} - \left(\frac{\sigma_{ij}^{intra}}{r_{ij}} \right)^{6} \right] \right) + \left(\frac{[q_i q_j]}{r_{ij}} \right) \end{aligned} \tag{S3}$$

where the first three harmonic potentials terms refer to stiff internal coordinates, whereas the fourth term is employed for flexible dihedrals and the last term takes into account selected non-bonded contributions between interacting atom pairs (N_{pairs}) within the same molecule. Similarly, we choose to express the intermolecular QMD-FF term through the standard sum of 12-6

Lennard-Jones (LJ) and charge-charge contributions:

$$u_{ij}^{inter} = 4\epsilon_{ij}^{inter}\left[\left(\frac{\sigma_{ij}^{inter}}{r_{ij}}\right)^{12} - \left(\frac{\sigma_{ij}^{inter}}{r_{ij}}\right)^{6}\right] + \frac{q_i q_j}{r_{ij}} \tag{S4}$$

where ϵ_{ij}^{inter} and σ_{ij}^{inter} are the LJ 12-6 parameters and q_i and q_j the point charges. It might be worth mentioning that the intra- and intermolecular LJ parameter sets $\epsilon_{ij}^{intra}/\sigma_{ij}^{intra}$ and $\epsilon_{ij}^{inter}/\sigma_{ij}^{inter}$ may take different values,[6–9] as they describe the interaction of the i and j atoms within the same molecule or between two separate monomers, respectively.

The parameterisation of the intramolecular QMD-FF for the investigated NFAs has been carried out, here and in previous work,[10] with the JOYCE code,[11] using DFT data purposely computed for the target compound. QM chemical descriptors are first computed for the isolated monomer, and exploited for the parameterization of the u^{intra} intramolecular term defined in Eq. (S4), retrieving the best parameters by minimizing the objective function[6,8,12]

$$I^{\text{JOYCE}} = \frac{1}{N_{geom}}\sum_{g}^{N_{geom}} W_g\left[\Delta E_{intra}^{QM} - u^{intra}\right]_g^2 + \sum_{K\leq L}^{3N-6}\frac{2W''_{KL}}{(3N-6)(3N-5)}\left[H_{KL}^{QM} - \left(\frac{\partial^2 u^{intra}}{\partial Q_K \partial Q_L}\right)\right]_{g=0}^2 \tag{S5}$$

The first sum runs over the N_{geoms} chain conformations retrieved from QM relaxed torsional energy scans, ΔE_{intra}^{QM} being the DFT internal energy. The second sum runs over the QM normal modes, H_{KL}^{QM} is the QM Hessian matrix evaluated at the equilibrium geometry ($g = 0$). W_g and W''_{KL} terms are user-defined weights which were set accordidng to previous applications.[9,13]

To retrieve the parameters specifying the intermolecular QMD-FF term, we employed the recently implemented PICKY-FRM automated procedure,[9] according to which the QMD-FF intermolecular term u^{inter} is parameterised as outlined in the following:

I) QMD-FF point charges are obtained at QM level, through the RESP procedure applied to the optimized geometry, accounting for the environment polarization through the continuum PCM model.[14]

II) Following the protocol designed for liquid crystals,[9] the LJ intermolecular parameters of the aliphatic chains are simply transferred from OPLS,[15] and constrained during the parameterization.

III) The remaining LJ parameters describing Y6 aromatic core are obtained through the iterative

PICKY-FRM protocol,[9] by minimising the standard objective function,[7,16,17]

$$I^{Picky} = \frac{1}{C}\sum_{i}^{N_{dim}} W_i \left[\Delta U_{inter}^{QM} - E_{inter}^{QMD-FF}\right]_i^2 \; ; \; C = \sum_{i}^{N_{dim}} W_i \tag{S6}$$

Further details about the parameterisation of the intermolecular term can be found in the original PICKY papers.[7,9,16,17]

Three different FFs were explored in this work, as discussed in the main text and summarised in Table 1. As far as the intramolecular QMD-FF parameterization is concerned, for the aromatic core, common to all substrates, we refer to our previously parameterised FF,[10] obtained fitting QM reference data with the JOYCE software.[11] Turning to the alkyl side chains, we parameterised intramolecular terms again following the JOYCE procedure, with reference data (Hessian, relaxed scans) obtained at B3LYP-D3/6-31G(d), while we transferred the intramolecular LJ terms from the OPLS force field.[18] In all cases, OPLS parameters were obtained through the LigParGen server.[15] We eventually obtained the desired FFs for the NFAs reported in Fig. 1 of the main manuscript, by replacing selected terminal atoms of the core with alkyl side chains of the appropriate length. The topology merge was carried out with home-made scripts, and missing stretching, bending, and torsional terms were added by hand using parameters transferred from the alkyl side chain parameterisation. We also added intramolecular LJ terms among side chains and between core and chains, to avoid undesired proximity. Each QMD-FF was completed with an inter-molecular term (Eq. S4), where the point charges were obtained according to the RESP procedure,[19] to the B3LYP-D3/6-31G(d) electrostatic potential of the entire molecule. Finally, the Lennard-Jones terms were parameterized following the above described Picky procedure,[9] based on the interaction energy of a large number of sampled dimers, evaluated at B3LYP-D3/6-31G(d) level of theory, after comparing results obtained with various functionals and basis sets. In total, we fitted 480 interaction energies sampled in both the attractive and repulsive regions of the LJ potential.

S1.3 MD simulations

To validate QMD-FFs obtained with the previously described strategy we ran classical MD simulations on crystals with the GROMACS 2020.5 software.[20] We generated a $3 \times 3 \times 3$ supercell starting from the experimental unit cell. The supercells contain 216 molecules in total ($\approx$ 40000-52000 atoms, depending on the system). We adopted periodic boundary conditions taking into account long range electrostatic effects through the PME algorithm.[21] We used an integration time step of 1 fs, imposing contraints on all bonds through the LINCS algorithm,[22] adopting a Berendsen thermostat to control temperature and an anisotropic Berendsen barostat to control

pressure.[23] The computational protocol consisted of an initial steepest descent minimisation of the supercell generated from the experimental crystal structure, followed by a slow NVT heating procedure starting from 25 K, initially carried out keeping aromatic cores frozen, and gradually releasing them once the target temperature (either 100 K or 293 K) was reached. After equilibrating the system at the target temperature in NVT conditions for 2 ns, we activated the anisotropic pressure coupling and let the system equilibrate for additional 2 ns. We finally carried out a production run in NPT conditions, for 10 ns, which was used to evaluate properties to be compared with experimental crystal structures. We carried out analyses on MD trajectories exploiting GROMACS tools and the MDAnalysis python library,[24–27] and report the results in Section S3.

S1.3.1 MD heating sequences

To further validate the QMD-FFs, their ability to reproduce the thermal stability along the NFA aggregates series[3] was assessed through simulated heating sequences, carried out for all substrates (and also with OPLS parameters for L8-BO) as described in the following. Starting from the last step described in Section S1.3, we heated the crystal in steps of 50 K up to 500 K. Each heating occurred gradually over 500 ps, and the system was equilibrated at each temperature for 4.5 ns. Starting from 530 K, we heated in steps of 20 K over 500 ps, equilibrating for 4.5 ns, until 630 K for a total of 10 temperatures scanned along a 50 ns MD simulation.

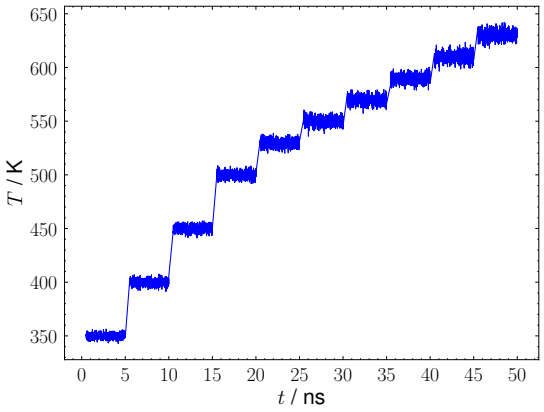

Fig. S1: Heating protocol adopted for thermal stability simulations.

The results for L8-BO, described with with either the OPLS force field or the QMD-FF, are reported in Fig. S11 and in Fig. S12, respectively. When adopting OPLS parameters, we start from a poorly structured crystal, as it is clear from the profile of the radial distribution function:

the peak at $r \approx 4$ Å is not very intense. Nonetheless, this short distance order is already completely lost upon heating to 400 K, while a small amount of long range order ($r \approx 8$ Å) persists up to 450-500 K. In this case, the order parameter P_2 is diagnostic of thermal instability, passing from $P_2 > 0.8$ at $T < 500$ K to $P_2 < 0.3$ at $T > 550$ K, a range where we can place the melting temperature obtained with the OPLS force field, hence severely underestimating the experimental value ($T_m = 593$ K) by 50-90 K.

When the same simulation is carried out with the QMD-FF, we notice a much more structured crystal in the radial distribution function, where a strong peak at $r \approx 4$ Å attributable to π-stacking, which significantly reduces upon heating up to ≈ 500 K, but persists without evident variations at higher temperatures. Despite much longer MD simulations,beyond the scope of this work, would be required to observe entirely the phase transition, both the progressive loss of medium- to long-range order, revealed by the broadening of the RDF signal at $r > 5$ Å, and the slight decrease of the order parameter P_2 at $T > 530$ K. We remark that the accurate simulation of the melting transition temperatures for all the substrates studied here would require much longer simulations, a task beyond the objectives of the current study. Nevertheless, this test clearly demonstrates the superior accuracy of our QMD-FFs, in terms of both thermodynamic and structural properties, in comparison to OPLS, which are determined by a more accurate description of both intra- and intermolecular potentials.

S1.4 Electronic calculations

To evaluate electronic properties on snapshots extracted from MD trajectories, we started from the last NVT step described in Section S1.3, and ran analogous 60 ns NVT production simulations, this time imposing LINCS constraints only on bonds involving hydrogen atoms, and switching temperature control to Bussi thermostat[28] Snapshots extracted every 500 ps from the last 40 ns of these trajectories were processed by cropping side chains after the first carbon atom, so as to leave the aromatic core substituted with methyl groups, in analogy to our previous work and to what similarly done by others,[4,10,29,30] before running electronic calculations at B3LYP-D3/6-31G* level, including environmental polarisation effects through the PCM model ($\varepsilon = 4$).[31] We computed electron transfer integrals between frontier orbitals as $J_{ij} = \langle \phi_i | \hat{F} | \phi_j \rangle$, where ϕ_i and ϕ_j are the unperturbed LUMO orbitals of the isolated monomers, respectively, and $\hat{F}$ is the Fock operator of the dimer.[10,32]

S2 Y6 core interaction energy curves

To assess that a parameterisation of non-bonded interactions for the Y6 core was necessary, we compared FF interaction energy curves, obtained by computing the intermolecular term S4 with

either the OPLS or the QMD-FF, with the QM values obtained with varied DFT descriptions for selected dimer geometries.

Concretely, based on the most probable configurations expected for the crystals, two intermolecular displacement were explored: the stacking distance r between the center of mass of the aromatic planes and the rotation β around the normal axis of the Y6 plane. For both coordinates, two different dimer arrangements were also considered, namely, for r, an anti parallel face-to-face arrangement (AFF, $\beta = 0$) and one obtained from the former by a β rotation of -15 ° (B-15), and, for β, two stacked arrangements at 4 Å (ROTB 4A) and at 4.3 Å (ROTB 4.3A).

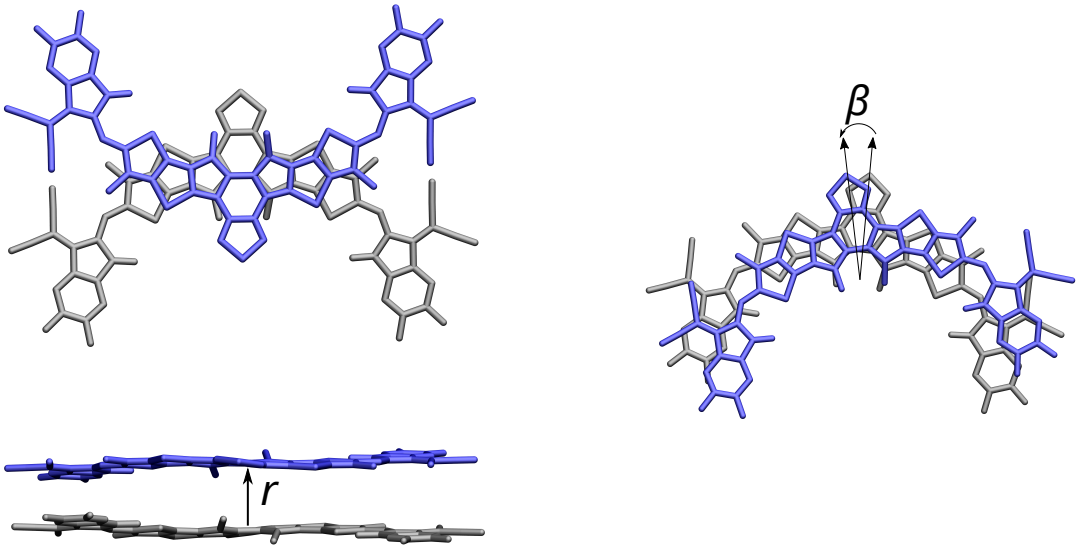

Fig. S2: Definition of Anti-face-to-face dimer arrangement (AFF, left) and rotation angle β used to explore rigid-body interaction curves.

In all cases, dimer geometries were obtained by displacing monomers within the rigid body approximation, using the equilibrium geometry obtained from DFT/B3LYP-D3/6-31G* optimisation. QM interaction energies have been also evaluated with other functionals and basis sets taking into account basis set superposition corrections, while OPLS interaction energies were evaluated from the non-bonded parameters we used in our previous work.[10] Finally, we report as a quantitative figure of merit for the comparison between the two sets of parameters the standard deviation between QM and MM interaction energies computed on the 480 sampled dimer geometries. For OPLS parameters, such value amounts to $\sigma = 10.98$ kJ mol^{-1}, while for the picky optimised parameters, we obtained $\sigma = 3.71$ kJ mol^{-1}.

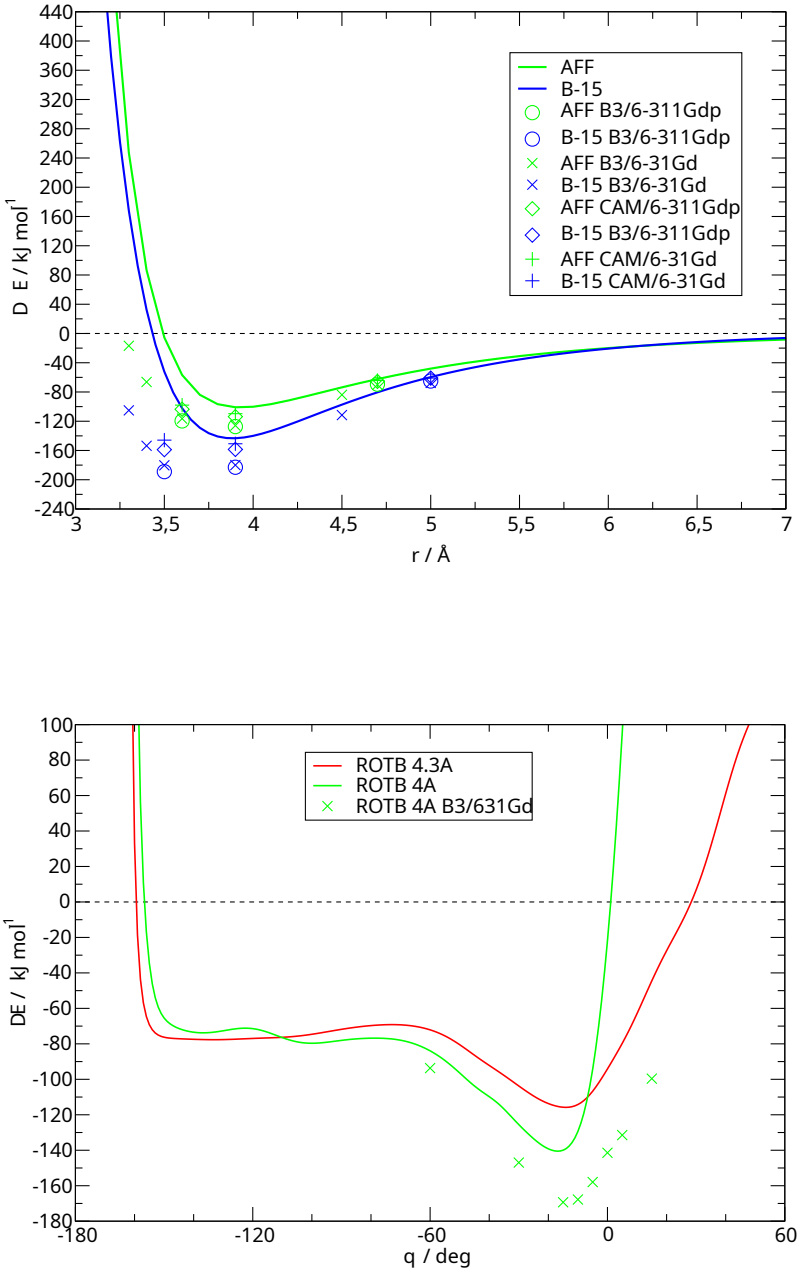

Fig. S3: QM (symbols) vs OPLS (lines) Lennard-Jones rigid-body interaction curves for Y6.

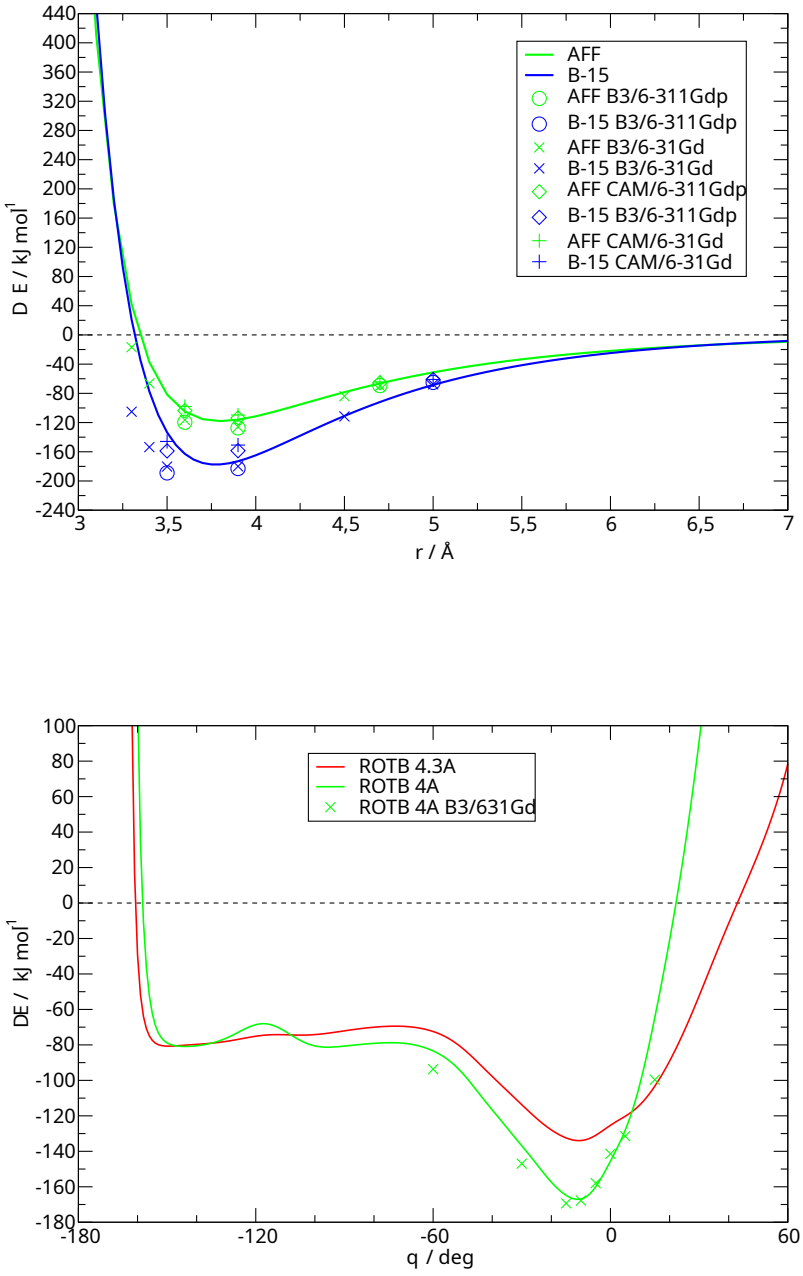

Fig. S4: QM (symbols) vs Picky (lines) Lennard-Jones rigid-body interaction curves for Y6.

S3 MD results

The uniaxial second rank order parameter $P_2^{\parallel}$ ($P_2^{\perp}$) was retrieved from the largest (smallest) eigenvalue of the Saupe ordering matrix Q, defined as[33–35]

$$Q_{ab} = \left\langle \frac{1}{2}(3\mathbf{u}_a\mathbf{u}_b - \delta_{ab}) \right\rangle \tag{S7}$$

where $\mathbf{u}$ ($a = x, y, z$) is the target molecule long axis, δ_{ab} the Kronecker delta and the mean value $\langle \ldots \rangle$ stands for an average over all molecules. The eigenvector associated to P_2 represents the phase director $\mathbf{n}$, and we can define $\alpha_i = \arccos(\mathbf{n} \cdot \mathbf{u}_i)$, *i.e.* the angle between the phase director $\mathbf{n}$ and the long molecular axis $\mathbf{u}_i$ of the i-th molecule. We can then compute the first and fourth rank order parameters P_1 and P_4 as

$$P_1 = \langle \cos\alpha \rangle \tag{S8}$$

$$P_4 = \left\langle \frac{1}{8}(35\cos^4\alpha - 30\cos^2\alpha + 3) \right\rangle \tag{S9}$$

where we performed an average over all molecules.

Table S1: Comparison between MD unit cell data for L8-BO obtained with three force fields.

Property	Expt. 150 K[3]	QMD-FF 293 K	Hyb-FF 293 K	OPLS 293 K
a / Å	27.704	29.54 ± 0.09	28.85 ± 0.09	26.3 ± 0.1
b / Å	20.855	20.89 ± 0.03	21.08 ± 0.04	21.68 ± 0.08
c / Å	28.363	26.64 ± 0.04	27.16 ± 0.04	29.63 ± 0.08
α / deg	90.0	90.0	90.0	90.0
β / deg	105.949	107.31 ± 0.06	106.65 ± 0.08	104.0 ± 0.1
γ / deg	90.0	90.0	90.0	90.0
V / Å^3	15 756	16 440 ± 19	16 513 ± 16	16 867 ± 25
ρ / kg m^{-3}	1248	1199 ± 1	1194 ± 1	1166 ± 2
$P_2^{\parallel core}$		0.955 ± 0.001	0.956 ± 0.001	0.921 ± 0.009
$P_4^{\parallel core}$		0.854 ± 0.003	0.857 ± 0.005	0.77 ± 0.02
$P_2^{\perp core}$		−0.500	−0.500	−0.484 ± 0.002
$P_4^{\perp core}$		0.374	0.374	0.337 ± 0.007

Table S2: Comparison between experimental and MD unit cell data for Y6.

Property	Expt. 100 K[1]	MD 100 K	MD 293 K
a / Å	15.112	15.75 ± 0.03	15.98 ± 0.02
b / Å	57.812	57.63 ± 0.04	57.95 ± 0.06
c / Å	20.076	17.21 ± 0.07	17.51 ± 0.03
α / deg	90.0	90.0	90.0
β / deg	95.923	97.15 ± 0.04	97.13 ± 0.02
γ / deg	90.0	90.0	90.0
V / Å^3	17 446	15 622 ± 40	16 226 ± 22
ρ / kg m^{-3}	1106	1238 ± 3	1192 ± 2
$P_2^{\parallel core}$		0.528 ± 0.001	0.553 ± 0.003
$P_4^{\parallel core}$		−0.127 ± 0.002	−0.095 ± 0.004
$P_2^{\perp core}$		−0.488 ± 0.001	−0.490 ± 0.002
$P_4^{\perp core}$		0.346 ± 0.002	0.351 ± 0.004

Table S3: Comparison between experimental and MD unit cell data for L8-BO.

Property	Expt. 150 K[3]	MD 100 K	MD 293 K
a / Å	27.704	28.26 ± 0.04	29.54 ± 0.09
b / Å	20.855	21.03 ± 0.01	20.89 ± 0.03
c / Å	28.363	25.97 ± 0.03	26.64 ± 0.04
α / deg	90.0	90.0	90.0
β / deg	105.949	107.05 ± 0.01	107.31 ± 0.06
γ / deg	90.0	90.0	90.0
V / Å^3	15 756	15 438 ± 36	16 440 ± 19
ρ / kg m^{-3}	1248	1277 ± 3	1199 ± 1
$P_2^{\parallel core}$		0.938 ± 0.002	0.955 ± 0.001
$P_4^{\parallel core}$		0.800 ± 0.006	0.854 ± 0.003
$P_2^{\perp core}$		−0.500	−0.500
$P_4^{\perp core}$		0.375	0.374

Table S4: Comparison between experimental and MD unit cell data for L8-HD.

Property	Expt. 150 K[3]	MD 100 K	MD 293 K
a / Å	24.680	25.39 ± 0.01	28.3 ± 0.3
b / Å	22.186	22.12 ± 0.02	20.2 ± 0.4
c / Å	32.616	31.23 ± 0.04	31.8 ± 0.3
α / deg	90.0	90.0	90.0
β / deg	106.818	107.26 ± 0.03	108.8 ± 0.2
γ / deg	90.0	90.0	90.0
V / Å^3	17 095	17 546 ± 7	18 208 ± 79
ρ / kg m^{-3}	1237	1208.5 ± 0.5	1165 ± 5
$P_2^{\parallel core}$		0.807 ± 0.002	0.90 ± 0.01
$P_4^{\parallel core}$		0.430 ± 0.006	0.68 ± 0.03
$P_2^{\perp core}$		−0.499	−0.497 ± 0.001
$P_4^{\perp core}$		0.373	0.368 ± 0.001

Table S5: Comparison between experimental and MD unit cell data for L8-OD.

Property	Expt. 150 K[3]	MD 100 K	MD 293 K
a / Å	24.799	24.63 ± 0.01	29.4 ± 0.6
b / Å	24.044	23.69 ± 0.02	23.4 ± 0.3
c / Å	33.623	32.03 ± 0.02	28.8 ± 0.3
α / deg	90.0	90.0	90.0
β / deg	110.385	109.92 ± 0.03	115.7 ± 0.5
γ / deg	90.0	90.0	90.0
V / Å^3	18 792	18 690 ± 8	19 831 ± 42
ρ / kg m^{-3}	1205	1214.3 ± 0.5	1144 ± 2
$P_2^{\parallel core}$		0.729 ± 0.001	0.757 ± 0.005
$P_4^{\parallel core}$		0.241 ± 0.003	0.31 ± 0.01
$P_2^{\perp core}$		−0.500	−0.498 ± 0.001
$P_4^{\perp core}$		0.374	0.371 ± 0.004

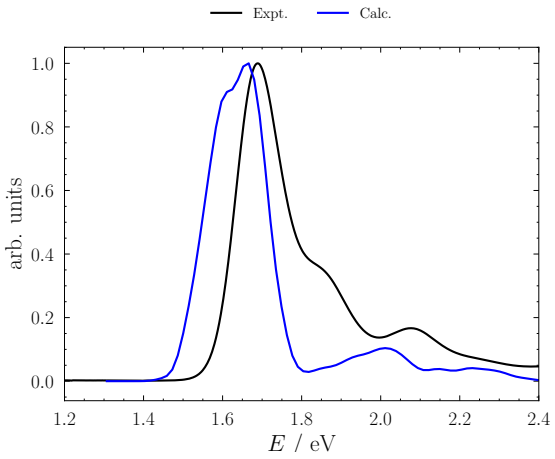

Fig. S5: Comparison between experimental absorption spectrum in choloroform,[36] and TDDFT/B3LYP-D3/6-31G* (PCM for chloroform) obtained from the convolution of the first three electronic transitions computed on 320 snapshots extracted from MD simulations.

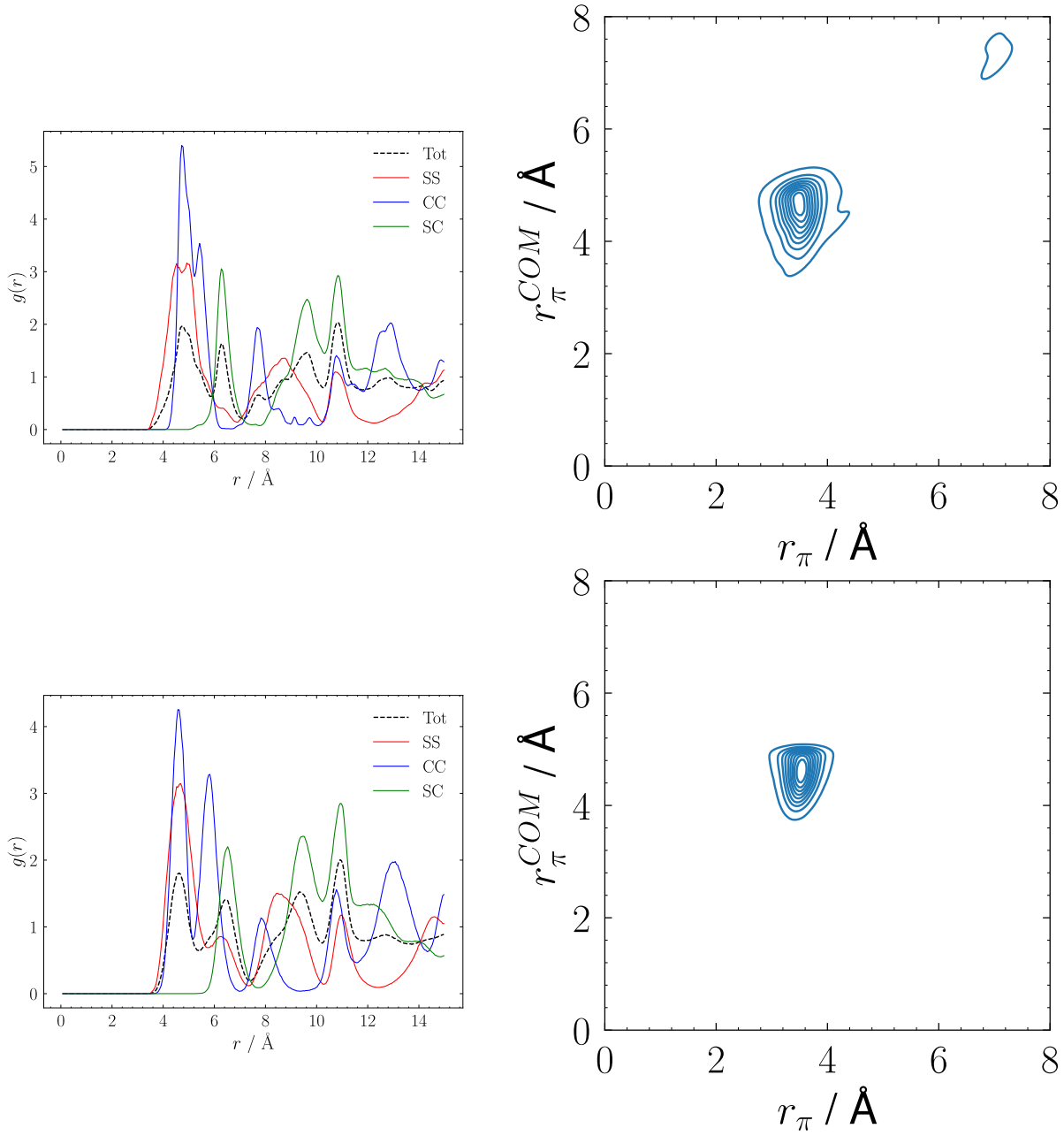

Fig. S6: 100 K (top) and 293 K (bottom) Radial Distribution Function (left) and stacking distance (right) among rings not belonging to the same molecule for Y6 10 ns MD simulation.

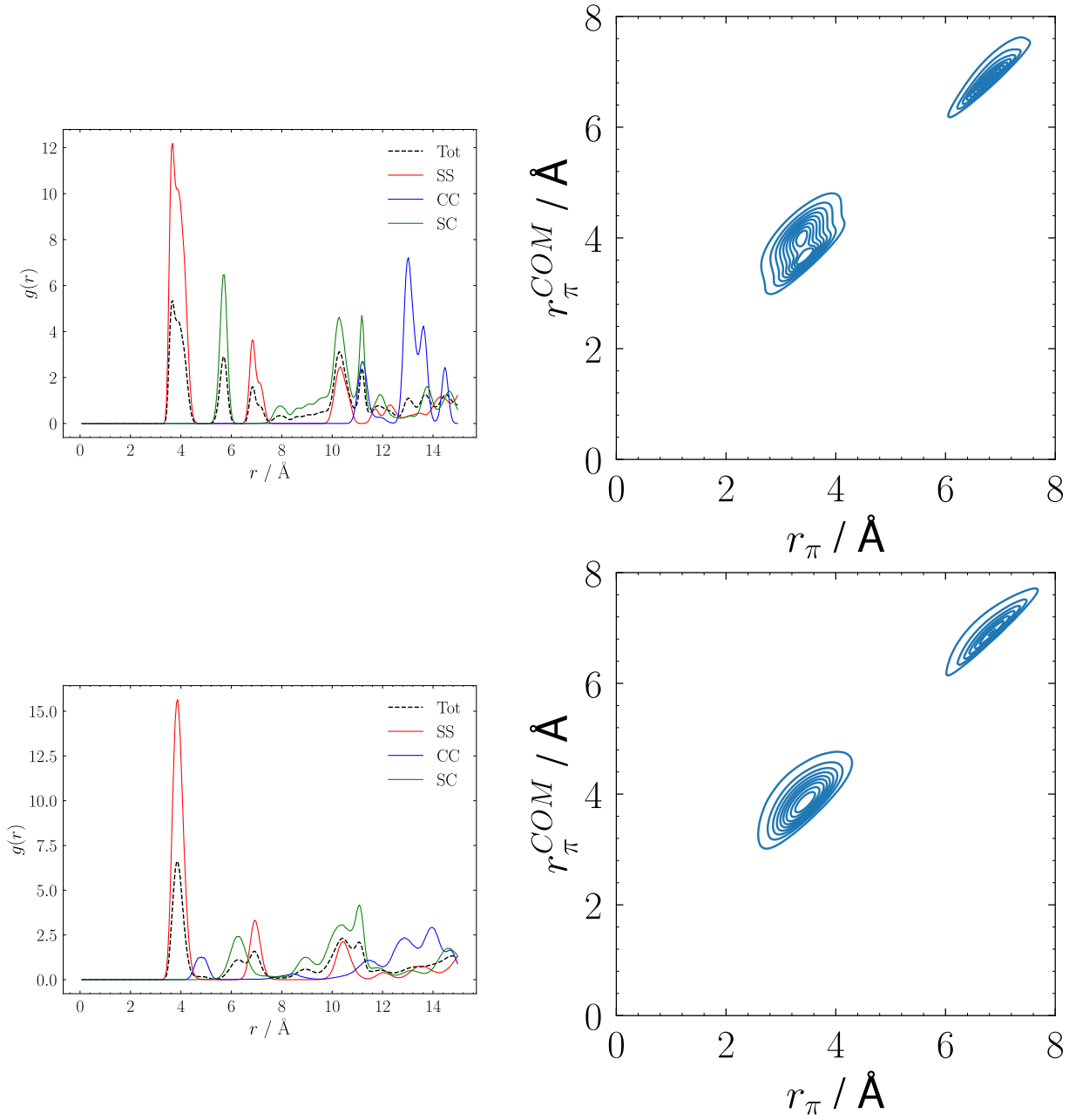

Fig. S7: 100 K (top) and 293 K (bottom) Radial Distribution Function (left) and stacking distance (right) among rings not belonging to the same molecule for L8-BO 10 ns MD simulation.

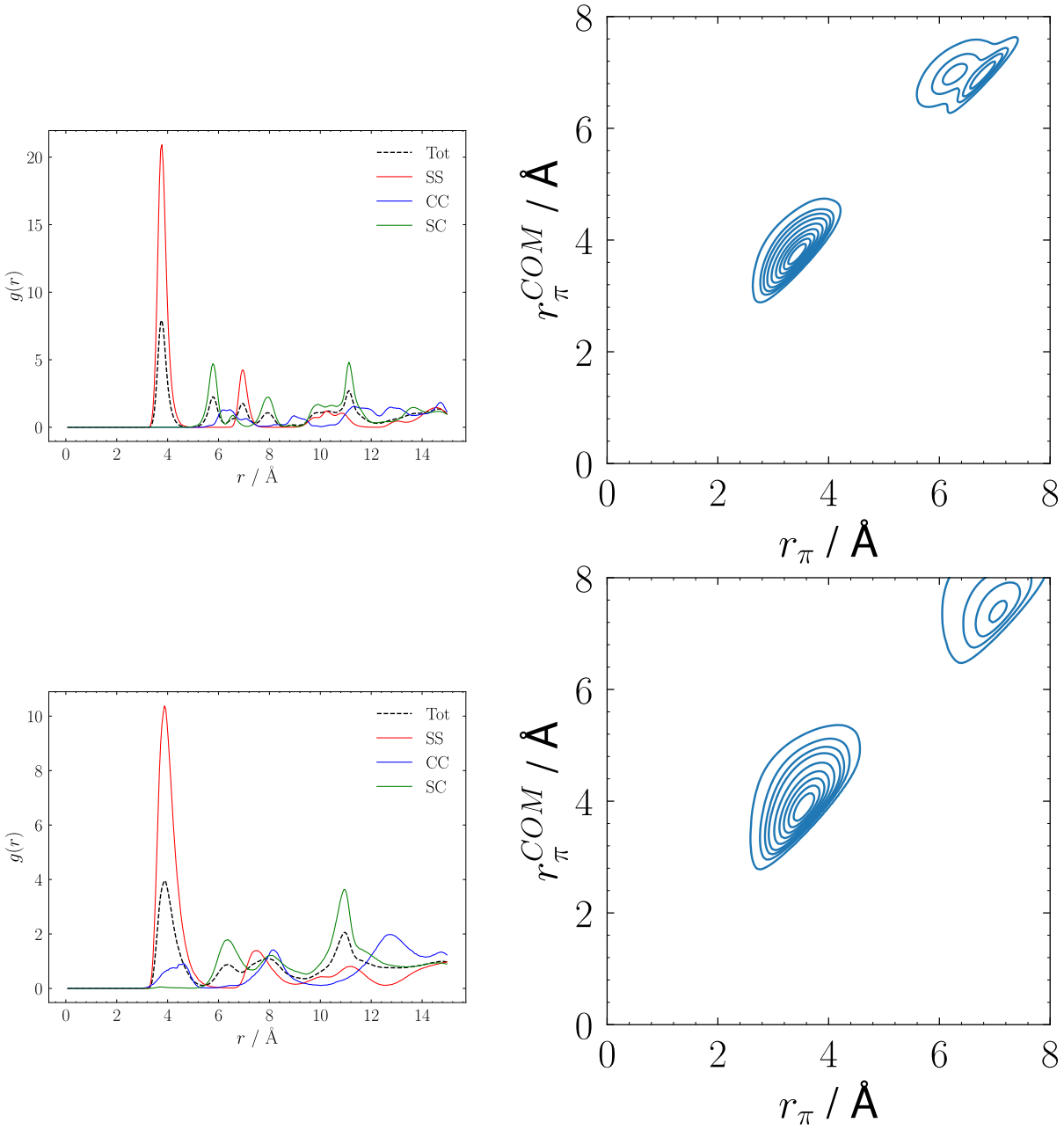

Fig. S8: 100 K (top) and 293 K (bottom) Radial Distribution Function (left) and stacking distance (right) among rings not belonging to the same molecule for L8-HD 10 ns MD simulation.

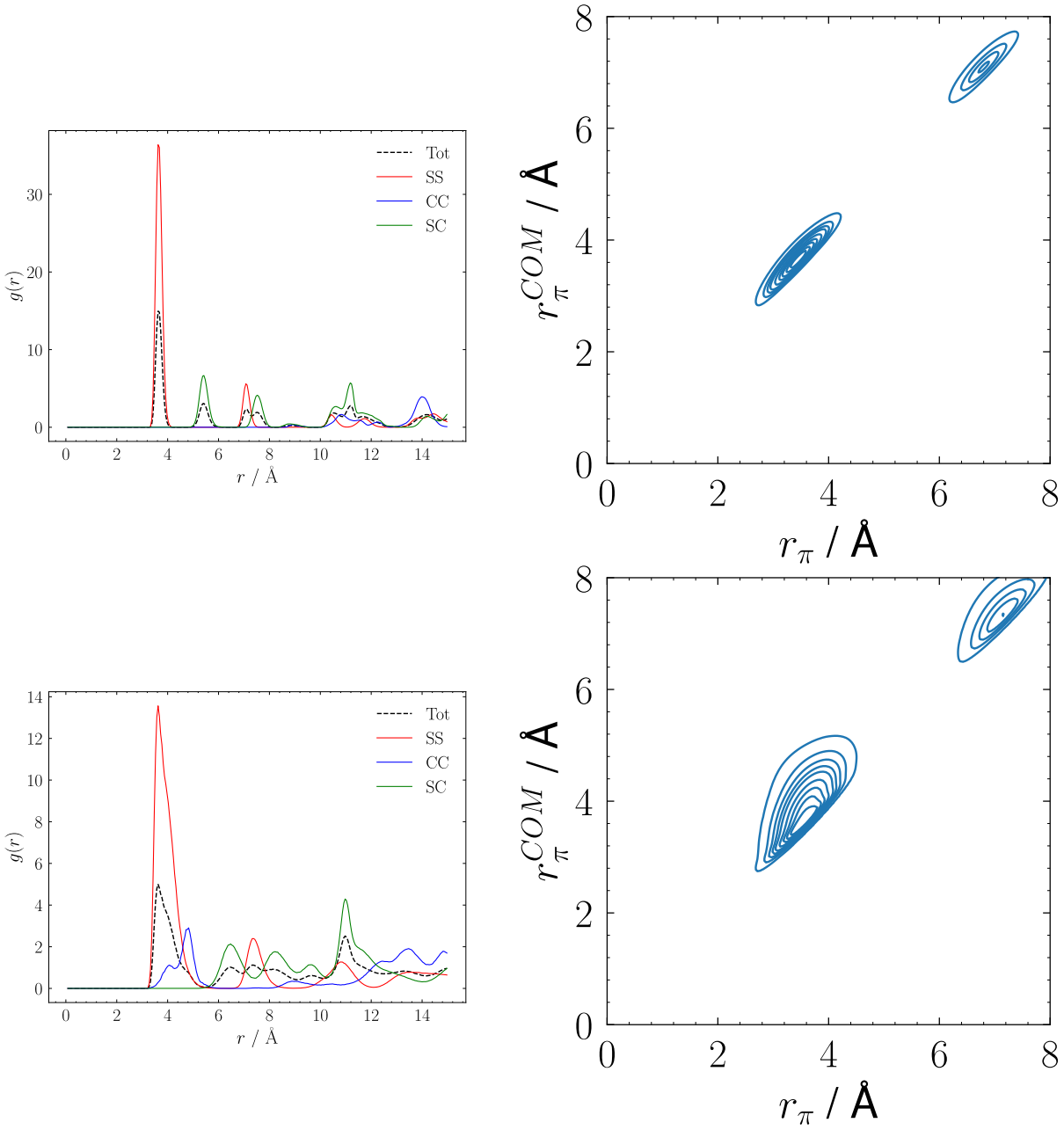

Fig. S9: 100 K (top) and 293 K (bottom) Radial Distribution Function (left) and stacking distance (right) among rings not belonging to the same molecule for L8-OD 10 ns MD simulation.

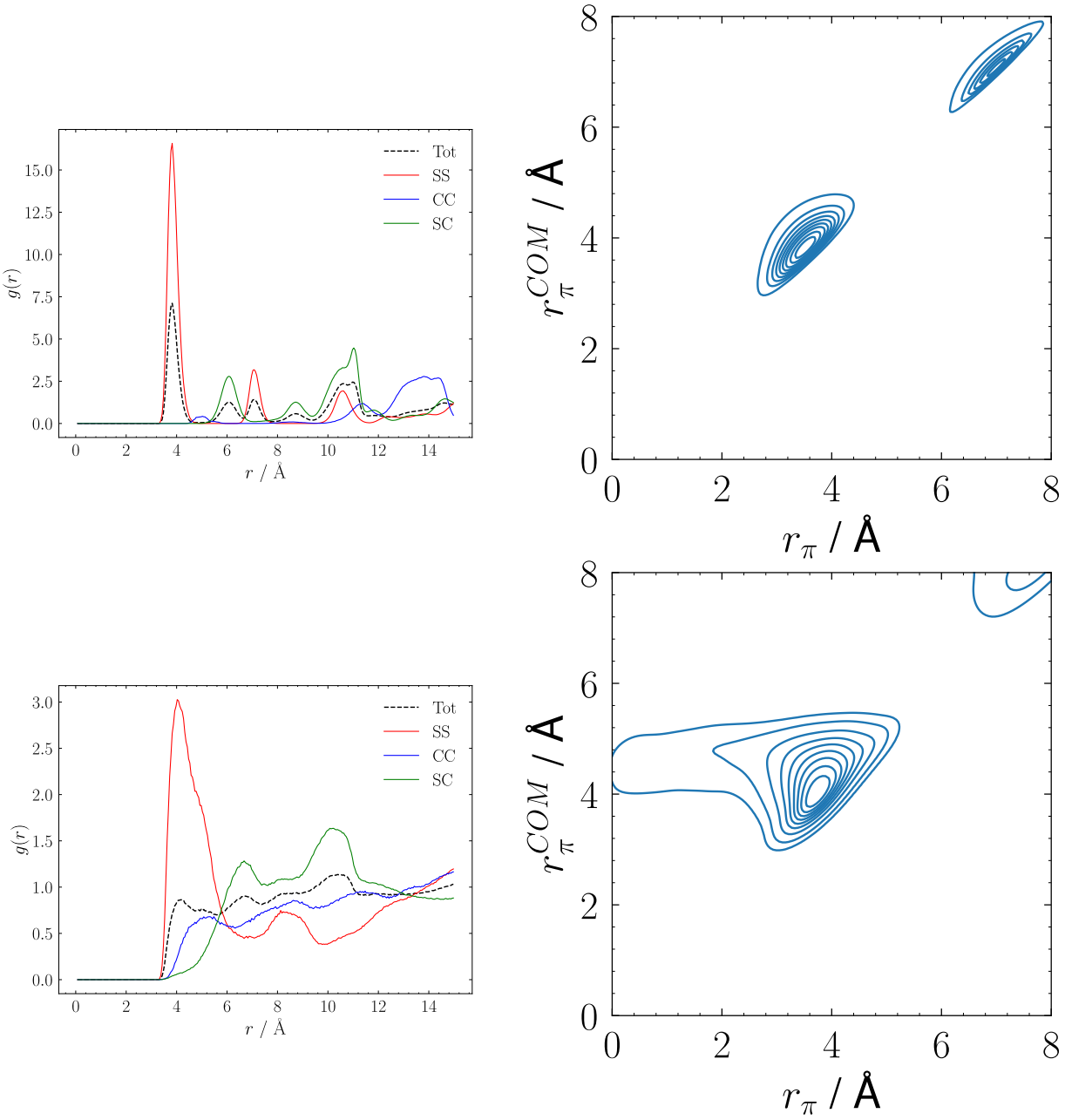

Fig. S10: Hybrid (top) and OPLS (bottom) Radial Distribution Function (left) and stacking distance (right) among rings not belonging to the same molecule for L8-BO 10 ns MD simulations at 293 K.

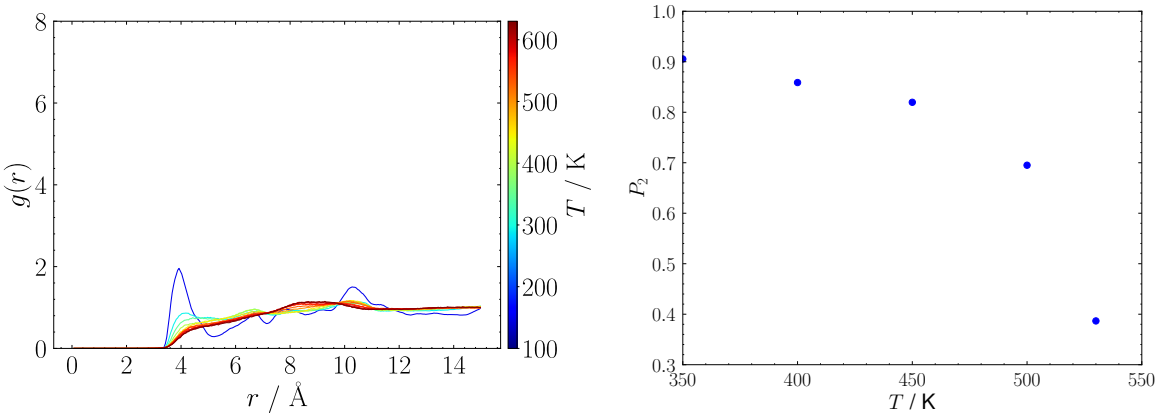

Fig. S11: Radial Distribution Function among rings not belonging to the same molecule (left), and P_2 order parameter (right) as a function of temperature for L8-BO MD simulations with OPLS.

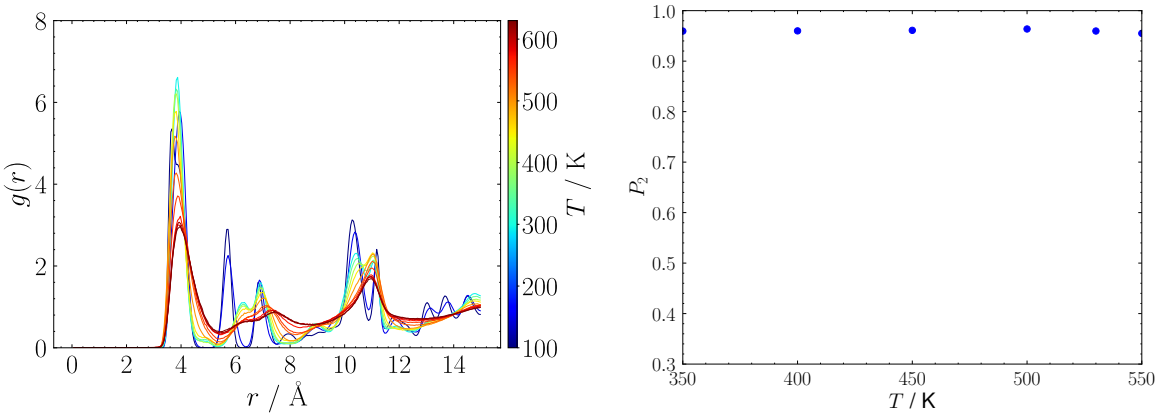

Fig. S12: Radial Distribution Function among rings not belonging to the same molecule (left), and P_2 order parameter (right) as a function of temperature for L8-BO MD simulations with QMD-FF.

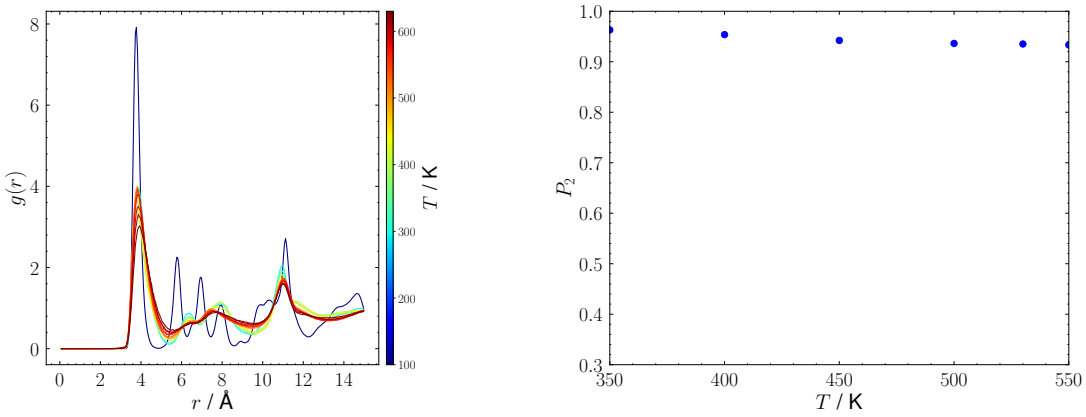

Fig. S13: Radial Distribution Function among rings not belonging to the same molecule (left), and P_2 order parameter (right) as a function of temperature for L8-HD MD simulations with QMD-FF.

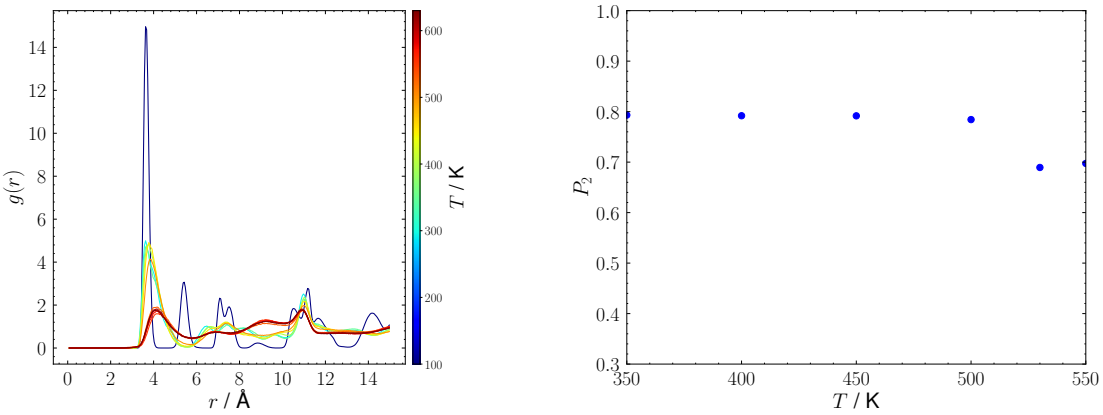

Fig. S14: Radial Distribution Function among rings not belonging to the same molecule (left), and P_2 order parameter (right) as a function of temperature for L8-OD MD simulations with QMD-FF.

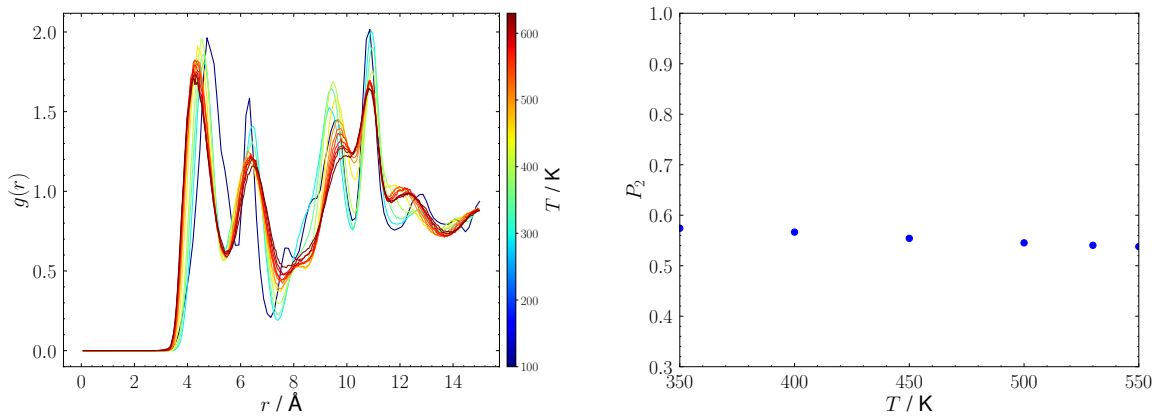

Fig. S15: Radial Distribution Function among rings not belonging to the same molecule (left), and P_2 order parameter (right) as a function of temperature for Y6 MD simulations with QMD-FF.

Table S6: Average RMSD from the best plane passing through the Y6 aromatic core along a 10 ns MD simulation.

Mol	RMSD $\pm\sigma$ / Å
Y6	1.88 ± 0.01
L8-BO	3.52 ± 0.01
L8-HD	2.80 ± 0.01
L8-OD	2.61 ± 0.02

S4 Evaluation of electron transfer integrals along MD

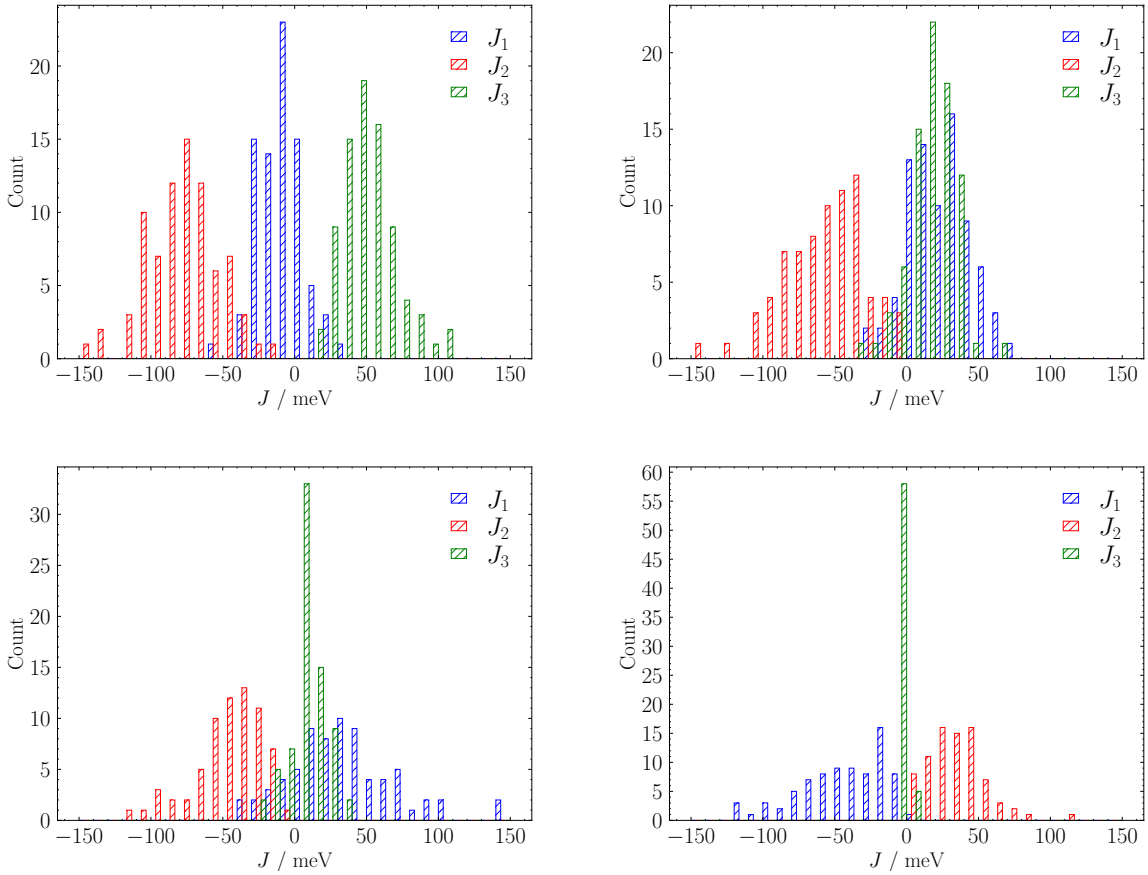

Fig. S16: Distribution of electron transfer integrals evaluated along MD trajectories at room temperature for L8-BO (top left), L8-HD (top right), L8-OD (bottom left), and Y6 (bottom right).

Table S7: Comparison between electron transfer integrals computed from experimental crystal structures and average values computed from classical MD trajectories.

NFA	Path	J^{X-ray} meV	J^{MD} meV	ΔJ meV
Y6	J_1	−59	−42	17
	J_2	18	34	16
	J_3	−15	0	15
L8-BO	J_1	−4	−6	−2
	J_2	45	−77	−122
	J_3	−82	49	131
L8-HD	J_1	5	24	19
	J_2	22	−57	−79
	J_3	−43	14	57
L8-OD	J_1	−18	35	53
	J_2	17	−44	−61
	J_3	46	7	−39

S5 Details on the Fermi's Golden Rule calculations

We evaluated rate constants by first order time-dependent perturbation theory, Fermi's Golden Rule (FGR), following Eq. 2 reported in the main text, where the FCWD $F(\Delta E_{ab}, T)$ is defined as:

$$F(\Delta E_{ab}, T) = \frac{1}{Z} \sum_{v_a, v_b} \mathrm{e}^{-\beta E_{v_i}} |\langle v_a | v_b \rangle|^2 \delta\left(E_{v_b} - E_{v_a} - \Delta E_{ab}\right) \tag{S10}$$

where $\langle v_a | v_b \rangle$ is the Franck-Condon integral, Z is the vibrational partition function of the initial electronic state, $\beta = 1/(k_\mathrm{B}T)$, and the sum runs over all vibrational states of $|a\rangle$ and $|b\rangle$.
Here, we have adopted the generating function (GF) approach for the evaluation of $F(\Delta E_{ab}, T)$,[37,38] which, in the framework of harmonic approximation for nuclear motion, allows to compute $F(\Delta E_{ab}, T)$ considering the whole set of the molecular normal modes of both initial and final states, taking into account the effects due to both changes of the equilibrium positions and of vibrational frequencies, as well as the effects due to normal mode mixing. The GF approach allows to handle the infinite summations appearing in Eq. S10 exploiting the integral representation of Dirac's delta function and Duschinsky's normal mode transformation:[39]

$$\mathbf{Q}_a = \mathbf{J}\mathbf{Q}_b + \mathbf{K} \tag{S11}$$

where **J** and **K** are the rotation matrix and the equilibrium displacement vector, respectively, while $\mathbf{Q}_a$ and $\mathbf{Q}_b$ are the normal coordinates of the electronic states $|a\rangle$ and $|b\rangle$.
We obtained Franck-Condon weighted densities of states (FCWDs) using a development version of the MolFC package,[40] using (TD-)DFT/B3LYP-D3/6-31G(d) for geometry optimisations and normal modes analyses. We adopted the curvilinear coordinate representation of normal modes, to prevent that large displacements of an angular coordinate could reflect into large shifts from the equilibrium positions of the involved bond distances. Such unphysical effect is unavoidable when using rectilinear coordinates and requires the use of high order anharmonic potentials for its correction.

S6 Evaluation of charge mobility along MD

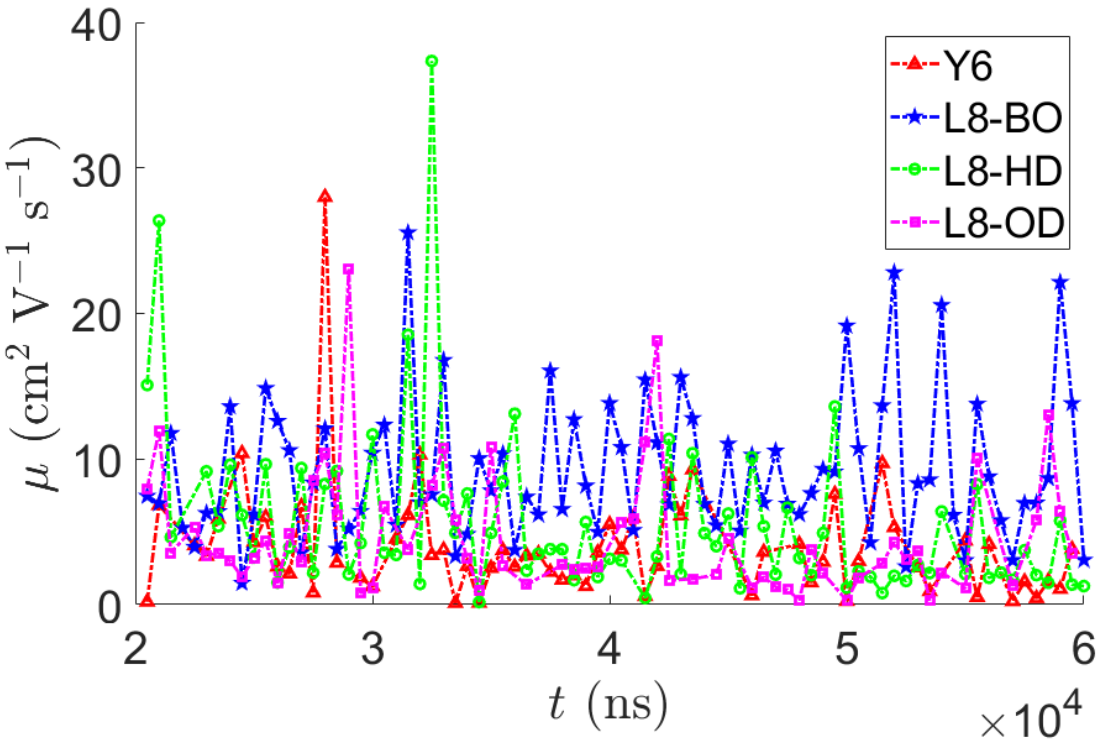

Fig. S17: Mobilities ($\mathrm{cm}^2\,\mathrm{V}^{-1}\,\mathrm{s}^{-1}$) evaluated along the MD trajectory at room temperature

The plot in Fig. S17 shows that, as expected, the mobility experiences strong fluctuations along the MD run. To gain further insight about the reasons behind this fluctuations, we have analysed the LUMO orbitals of the dimers for the snapshot with the highest or lowest mobility, identifying

the sliding between monomers as the main reason for the significant variation in the mobility value, as shown in Fig. S18.

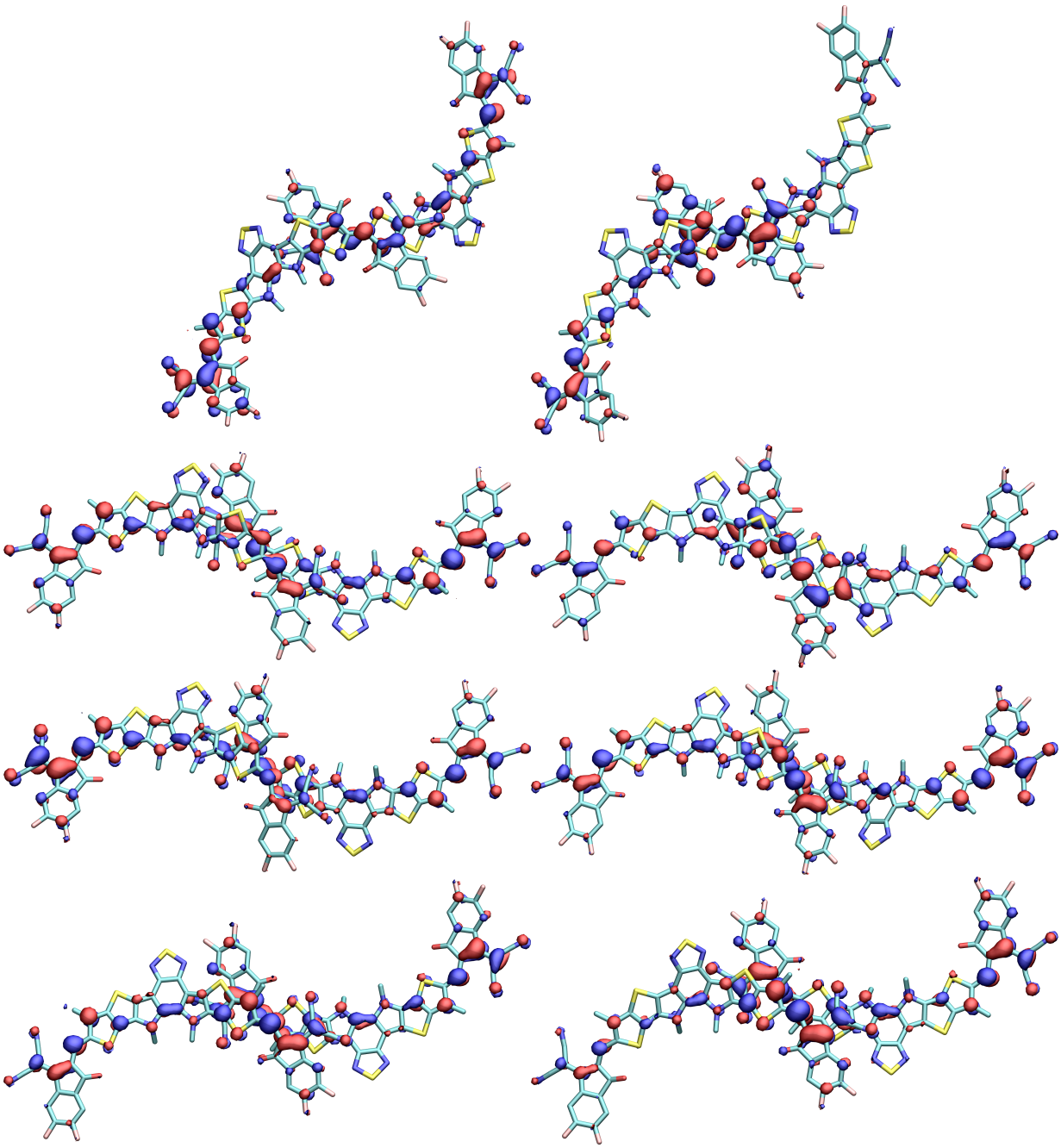

Fig. S18: LUMO orbitals for the pair 1-4 of Y6 (first row), and 1-109 of L8-BO, L8-HD, and L8-OD (second, third, and fourth rows, respectively) in their minimum (left) and maximum (right) mobility arrangements found along the MD trajectory. Side chains omitted for clarity.

Inspection of Fig. S18 shows that the very different mobility is related to a small slide of the interacting molecules. Indeed, while in the right panel they are disposed so that there is an in-phase interaction between the LUMOs. Conversely, in the left panel it is easy to see that the lobes of the upper molecule insist over the nodes of the LUMO of the bottom molecule, so that, in the end, the in-phase and the opposite-phase interactions partially cancel each other leading to a very low value of the electronic coupling.

References

[S1] W. Zhu, A. P. Spencer, S. Mukherjee, J. M. Alzola, V. K. Sangwan, S. H. Amsterdam, S. M. Swick, L. O. Jones, M. C. Heiber, A. A. Herzing, G. Li, C. L. Stern, D. M. DeLongchamp, K. L. Kohlstedt, M. C. Hersam, G. C. Schatz, M. R. Wasielewski, L. X. Chen, A. Facchetti and T. J. Marks, *J. Am. Chem. Soc.*, 2020, **142**, 14532–14547.

[S2] C. R. Groom, I. J. Bruno, M. P. Lightfoot and S. C. Ward, *Acta Cryst. B*, 2016, **72**, 171–179.

[S3] C. Li, J. Zhou, J. Song, J. Xu, H. Zhang, X. Zhang, J. Guo, L. Zhu, D. Wei, G. Han, J. Min, Y. Zhang, Z. Xie, Y. Yi, H. Yan, F. Gao, F. Liu and Y. Sun, *Nat Energy*, 2021, **6**, 605–613.

[S4] G. Zhang, X.-K. Chen, J. Xiao, P. C. Y. Chow, M. Ren, G. Kupgan, X. Jiao, C. C. S. Chan, X. Du, R. Xia, Z. Chen, J. Yuan, Y. Zhang, S. Zhang, Y. Liu, Y. Zou, H. Yan, K. S. Wong, V. Coropceanu, N. Li, C. J. Brabec, J.-L. Bredas, H.-L. Yip and Y. Cao, *Nat. Commun.*, 2020, **11**, 3943.

[S5] C. Xiao, C. Li, F. Liu, L. Zhang and W. Li, *J. Mater. Chem. C*, 2020, **8**, 5370–5374.

[S6] I. Cacelli and G. Prampolini, *J. Chem. Theory Comput.*, 2007, **3**, 1803–1817.

[S7] I. Cacelli, A. Cimoli, P. R. Livotto and G. Prampolini, *J. Comput. Chem.*, 2012, **33**, 1055.

[S8] J. Cerezo, G. Prampolini and I. Cacelli, *Theor. Chem. Acc.*, 2018, **137**, 80.

[S9] J. G. Vilhena, L. Greff da Silveira, P. R. Livotto, I. Cacelli and G. Prampolini, *J. Chem. Theory Comput.*, 2021, **17**, 4449–4464.

[S10] A. Landi and D. Padula, *J. Mater. Chem. A*, 2021, **9**, 24849–24856.

[S11] I. Cacelli, J. Cerezo, N. De Mitri and G. Prampolini, JOYCE*2.10, a Fortran 77 code for intra-molecular force field parameterization, available free of charge at http://www.iccom.cnr.it/en/joyce-2/, last consulted May 2022*, 2019.

[S12] V. Barone, I. Cacelli, N. De Mitri, D. Licari, S. Monti and G. Prampolini, *Phys. Chem. Chem. Phys.*, 2013, **15**, 3736–51.

[S13] N. De Mitri, S. Monti, G. Prampolini and V. Barone, *J. Chem. Theory Comput.*, 2013, **9**, 4507–4516.

[S14] J. Tomasi, B. Mennucci and R. Cammi, *Chem. Rev.*, 2005, **105**, 2999–3094.

[S15] L. S. Dodda, I. Cabeza de Vaca, J. Tirado-Rives and W. L. Jorgensen, *Nucleic Acids Research*, 2017, **45**, W331–W336.

[S16] G. Prampolini, P. R. Livotto and I. Cacelli, *J. Chem. Theory Comput.*, 2015, **11**, 5182–96.

[S17] L. Greff Da Silveira, M. Jacobs, G. Prampolini, P. R. Livotto and I. Cacelli, *J. Chem. Theory Comput.*, 2018, **14**, 4884–4900.

[S18] W. L. Jorgensen, D. S. Maxwell and J. Tirado-Rives, *J. Am. Chem. Soc.*, 1996, **118**, 11225–11236.

[S19] C. I. Bayly, P. Cieplak, W. Cornell and P. A. Kollman, *J. Phys. Chem.*, 1993, **97**, 10269–10280.

[S20] M. J. Abraham, T. Murtola, R. Schulz, S. Páll, J. C. Smith, B. Hess and E. Lindahl, *SoftwareX*, 2015, **1-2**, 19–25.

[S21] T. Darden, D. York and L. Pedersen, *J. Chem. Phys.*, 1993, **98**, 10089–10092.

[S22] B. Hess, H. Bekker, H. J. C. Berendsen and J. G. E. M. Fraaije, *J. Comput. Chem.*, 1997, **18**, 1463–1472.

[S23] H. J. C. Berendsen, J. P. M. Postma, W. F. van Gunsteren, A. DiNola and J. R. Haak, *J. Chem. Phys.*, 1984, **81**, 3684–3690.

[S24] R. Gowers, M. Linke, J. Barnoud, T. Reddy, M. Melo, S. Seyler, J. Domański, D. Dotson, S. Buchoux, I. Kenney and O. Beckstein, Proceedings of the 15th Python in Science Conference, 2016.

[S25] N. Michaud-Agrawal, E. J. Denning, T. B. Woolf and O. Beckstein, *J. Comput. Chem.*, 2011, **32**, 2319–2327.

[S26] D. L. Theobald, *Acta Crystallogr. Sect. A: Found. Crystallogr.*, 2005, **61**, 478–480.

[S27] P. Liu, D. K. Agrafiotis and D. L. Theobald, *J. Comput. Chem.*, 2009, **31**, 1561–1563.

[S28] G. Bussi, D. Donadio and M. Parrinello, *The Journal of Chemical Physics*, 2007, **126**, 014101.

[S29] Z.-W. Zhao, Ö. H. Omar, D. Padula, Y. Geng and A. Troisi, *J. Phys. Chem. Lett.*, 2021, **12**, 5009–5015.

[S30] A. S. Gertsen, M. K. Sørensen and J. W. Andreasen, *Phys. Rev. Mater.*, 2020, **4**, 075405.

[S31] T. Nematiaram, D. Padula and A. Troisi, *Chem. Mater.*, 2021, **33**, 3368–3378.

[S32] T. Nematiaram, D. Padula, A. Landi and A. Troisi, *Adv. Funct. Mater.*, 2020, **30**, 2001906.

[S33] P. G. deGennes and J. Prost, *The Physics of Liquid Crystals* - second edition, Oxford University Press, Oxford, 1993.

[S34] C. Zannoni, *Liquid Crystals*, 2018, **45**, 1880–1893.

[S35] M. P. Allen, *Mol. Phys.*, 2019, **117**, 2391–2417.

[S36] X. Zou, G. Wen, R. Hu, G. Dong, C. Zhang, W. Zhang, H. Huang and W. Dang, *Molecules*, 2020, **25**, 4118.

[S37] R. Kubo and Y. Toyozawa, *Prog. Theor. Phys.*, 1955, **13**, 160–182.

[S38] M. Lax, *J. Chem. Phys.*, 1952, **20**, 1752–1760.

[S39] R. Borrelli and A. Peluso, *WIREs: Comput. Mol. Sci.*, 2013, **3**, 542–559.

[S40] R. Borrelli and A. Peluso, *MolFC: A program for Franck-Condon integrals calculation*, Package available online at `http://www.theochem.unisa.it`.